HHS Public Access

Author manuscript

ACS Nano. Author manuscript; available in PMC 2023 February 23.

Published in final edited form as:

ACS Nano. 2022 June 28; 16(6): 8820–8826. doi:10.1021/acsnano.1c09800.

Opto-Thermocapillary Nanomotors on Solid Substrates

Jingang Li[#],
Materials Science and Engineering Program and Texas Materials Institute, The University of Texas at Austin, Austin, Texas 78712, United States

Pavana Siddhartha Kollipara[#],
Walker Department of Mechanical Engineering, The University of Texas at Austin, Austin, Texas 78712, United States

Ya Liu,
State Key Laboratory of Multiphase Flow in Power Engineering, Xi'an Jiaotong University, Xi'an, Shaanxi 710049, China

Kan Yao,
Walker Department of Mechanical Engineering, The University of Texas at Austin, Austin, Texas 78712, United States

Yaoran Liu,
Department of Electrical and Computer Engineering, The University of Texas at Austin, Austin, Texas 78712, United States

Yuebing Zheng
Materials Science and Engineering Program and Texas Materials Institute, The University of Texas at Austin, Austin, Texas 78712, United States; Walker Department of Mechanical Engineering and Department of Electrical and Computer Engineering, The University of Texas at Austin, Austin, Texas 78712, United States

Abstract

Motors that can convert different forms of energy into mechanical work are of profound importance to the development of human societies. The evolution of micromotors has stimulated many advances in drug delivery and microrobotics for futuristic applications in biomedical engineering and nanotechnology. However, further miniaturization of motors toward the nanoscale is still challenging because of the strong Brownian motion of nanomotors in liquid environments. Here, we develop light-driven opto-thermocapillary nanomotors (OTNM) operated on solid substrates where the interference of Brownian motion is effectively suppressed. Specifically, by optically controlling particle–substrate interactions and thermocapillary actuation, we demonstrate the robust orbital rotation of 80 nm gold nanoparticles around a laser beam on a solid substrate.

Corresponding Author: Yuebing Zheng – *Materials Science and Engineering Program and Texas Materials Institute, The University of Texas at Austin, Austin, Texas 78712, United States; Walker Department of Mechanical Engineering and Department of Electrical and Computer Engineering, The University of Texas at Austin, Austin, Texas 78712, United States,* zheng@austin.utexas.edu.

[#]Author Contributions

J.L. and P.S.K. contributed equally to this work.

Complete contact information is available at: https://pubs.acs.org/10.1021/acsnano.1c09800

The authors declare no competing financial interest.

With on-chip operation capability in an ambient environment, our OTNM can serve as light-driven engines to power functional devices at the nanoscale.

Graphical Abstract

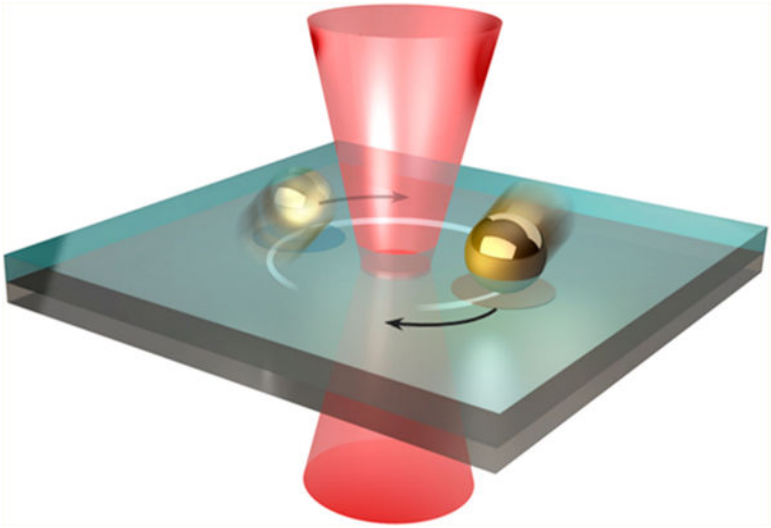

Keywords

optical nanomotors; nanoparticles; optical nanorotors; asymmetry; optical manipulation

INTRODUCTION

Micromotors have attracted tremendous interest because of their promising applications in microrobotics,[1,2] nanofabrication,[3,4] and biomedical engineering.[5–8] They can be driven by chemical reactions[9,10] and external stimuli, including electric,[11,12] magnetic,[13,14] light,[15–19] and acoustic fields.[20,21] Among them, light is regarded as an attractive stimulus for on-demand control of micromotors in a reversible and remote manner with excellent temporal and spatial resolution. For instance, photocatalytic reactions, which occur at the surface of a particle, can power asymmetric micromotors through self-diffusiophoresis,[22,23] self-electrophoresis,[17,24] and bubble propulsion.[25,26] In addition, optical forces and torques are widely exploited to drive micromotors. The spin angular momentum or orbital angular momentum carried by circularly polarized light or structured light can induce an optical torque to drive rotary micromotors.[27–30] The optical torque can also stem from the asymmetric scattering of exotically shaped nanostructures with linearly polarized light.[31] In addition, optothermal micromotors have been realized via laser-heating-induced thermophoresis,[32,33] thermoelectricity,[34,35] and demixing of critical mixtures.[36]

Despite the tremendous progress in light-driven micromotors, the miniaturization of motors toward the nanoscale, especially with all dimensions below 100 nm, remains challenging. Molecular machines have been proposed to control mechanical forces and motions at the molecular scale.[37] However, the strong reliance on molecular chemistry, the extremely localized motion, and the difficulty of real-time monitoring and control limit the broader

applications of molecular machines in solid-state devices. To overcome these limitations, nanomotors with the size ranging from 10 to 100 nm are essential in bridging the gap between micromotors and molecular motors. Different from optical tweezers that trap nanoparticles at a specific location, optical nanomotors move along a designed path. Thus, at such a small scale, precise control of the motion of nanomotors becomes challenging because of the dominance of random Brownian motion in the liquid environments.[2,38]

RESULTS AND DISCUSSION

Working mechanisms of OTNM.

Herein, we develop an opto-thermocapillary nanomotor (OTNM) in which the interference of Brownian motion is significantly suppressed. OTNM is operated on a solid substrate under ambient conditions, which is enabled by the rational optical modulation of particle–substrate interactions (see Figure S1 for the experimental setup). A thermally responsive layer of solid cetyltrimethylammonium chloride (CTAC) is sandwiched between the glass substrate and gold nanoparticles (AuNPs) as the nanomotors. When the laser is on, optical heating of the AuNP leads to a localized phase transition of CTAC from a crystalline structure to a quasi-liquid phase,[39,40] which generates the thermocapillary stress at the AuNP-CTAC interface to enable the rotary motion (Figure 1a). Figure 1b shows the real-time rotation of an 80 nm AuNP under laser excitation (Movie S1). An off-resonance laser wavelength at 660 nm was selected to avoid strong optical scattering forces to push the AuNP away from the laser beam. The AuNP rotates stably in a circular orbit around the laser beam (Figure 1c), as further indicated by the sinusoidal curve fitting of the laser–particle displacement along the X and Y axes (Figure 1d). It should be noted that the phase transition of CTAC is reversible, which leaves no trace of the motion on the CTAC film. This result contrasts with the light-driven, self-traced motion of AuNPs through optothermal milling of polymer films[41] or photocatalytic etching of silicon surfaces.[42]

To understand the working mechanisms of OTNM, we analyzed the in-plane forces in both radial and tangential directions (see Note S2 for ruling out the out-of-plane rolling). It should be noted that light sources used in this work are linearly polarized without additional optics for wavefront shaping. Thus, the angular momentum of light is not a viable driving force for the rotation of nanoparticles. We first took the scanning transmission electron microscope (STEM) images of the 80 nm Au nanomotors to gain their geometrical information (Figure 2a and Figure S2). The AuNPs were not in a perfectly spherical shape, and multifaceted asymmetry could be clearly observed. This asymmetry is essential in the origin of driving forces for the nanomotors, which will be discussed in detail in the following contents. As a control example, we also conducted experiments with ultrauniform gold nanospheres (diameter ~100 nm) and no rotation behaviors were observed (see Movie S2). To better understand the role of asymmetry, we developed a three-dimensional (3D) reconstruction method to build asymmetric AuNPs from STEM images and implemented the 3D asymmetric models in numerical simulations (Figure 2b, also see Figure S3 and Figure S4). Instead of retrieving the geometry of an individual nanoparticle, this approach enables the construction of multiple morphologies to resemble a batch of nanoparticles (see Note S1).

We then simulated the optical forces exerted on the AuNP using a finite-difference time-domain (FDTD) method (see Note S3). The tangential component of the in-plane optical force arising from the geometric asymmetry is too small to drive the rotation (Figure S5). Here, we ascribe the driving force of OTNM to the thermocapillary forces. Under laser excitation, optical heating of the AuNP leads to a localized temperature increase (Figure 2d). The elevated temperature is higher than the phase transition temperature of CTAC (~80 °C),[43] which results in a local phase transition of CTAC from the solid phase to a quasi-liquid structure. Because of the multifaceted asymmetry of the AuNP, a temperature gradient exists at the interface between the AuNP and quasi-liquid CTAC (Figure 2e). This nonuniform temperature results in an interfacial surface tension gradient (Figure S6), which generates localized nonzero thermocapillary stress at the AuNP-CTAC interface and a net thermocapillary force along the tangential direction of the AuNP (see Note S4 for more details).[44] The thermocapillary stress arises from the minuscule temperature variation on the AuNP surface with a multifaceted geometry (arrows in Figure 2f, also see Figure S7). In contrast, for a perfectly spherical AuNP, this thermocapillary stress vanishes in the in-plane direction because of the uniform temperature distribution, causing no rotation of the AuNP (see Movie S2). The direction of the local temperature gradient depends strongly on the surface asymmetry of the AuNP. Therefore, the direction of the asymmetry-induced thermocapillary forces is mainly dependent on the orientation of the AuNP, whereas the magnitude depends on both the orientation of the particle and the laser–particle distance (Figure S8).

As shown in the force analysis (Figure 2c), OTNM is enabled by the synergy of optical forces and thermocapillary forces. During the steady rotation, the radial components of optical and thermocapillary forces are balanced as the net centripetal force is orders of magnitude smaller because of low inertia of AuNPs. The radial optical force on the AuNP is only determined by the radial position, whereas the radial thermocapillary force also varies with the particle orientation. Thus, the AuNP continuously orients itself with respect to the laser–particle line to maintain a stable orientation throughout the circular rotation. To understand this self-orientation behavior, we calculated the total in-plane torques acting on the AuNP that is responsible for the orientational change. As shown in Figure 2g, there are two equilibrium orientations (indicated by the red arrows) where the total torque is zero and restoring torques exist once the orientation changes. It should be noted that only one orientation angle could lead to rotation of the AuNP whereas the other drives the AuNP away from the orbital track (Figure S9a).

Next, we evaluated the total radial and tangential forces exerted on the AuNP at the equilibrium orientation (Figure 2h). In the radial direction, the repelling thermocapillary force and the attractive optical force are balanced (Figure S9b), leading to an equilibrium laser–particle distance at ~420 nm, which is consistent with the experimental rotation radius (Figure 1c). The calculated energy potential (red curve) in the radial direction also indicates that the AuNP could be confined at the equilibrium position. It should be noted that although the width of the potential is large, the localized phase transition and high viscosity of quasi-liquid CTAC can effectively reduce the Brownian motion to retain stable orbital rotation. In the tangential direction, a thermocapillary driving force of ~15 fN is obtained, which is consistent with the magnitude of resistant drag forces (Note S5).

Modeling of OTNM.

To validate the proposed working mechanisms, we developed a physical model to numerically analyze the motion of the AuNP (Note S6). We considered an asymmetric AuNP interacting with a 660 nm laser. The AuNP experienced thermocapillary forces, optical forces, resistant drag forces, and torques as a function of the position and orientation of the AuNP, which were obtained from numerical simulations and analytical methods. At the initial time, the AuNP was placed at a random position with random orientation (Figure 3a). Because of the large restoring torque acting on the particle, the AuNP reoriented itself toward the equilibrium orientation during the first couple of milliseconds. Then, within 0.3 s, the AuNP was dragged toward the circular orbital while simultaneously maintaining at the equilibrium in-plane orientation induced by the restoring torques (Figure 3b,c). Subsequently, the AuNP started to stably rotate along the laser beam in a circular orbit (Figure 3d, also see Movie S3). The trajectory and velocity of the AuNP matched well with the experimental results in Figure 1c. In the real case, there exist perturbations in the system caused by the fluctuation of laser power, nonuniformity in the CTAC layer, and the vibration of the stage. To better represent the actual experimental behavior, we added noise in the model to mimic the experimental fluctuations (see Note S6). In the presence of noise, the AuNP rotated in the circular orbit with some position fluctuations, which is similar to the experimental results (Figure S10 and Movie S4). The replication of experimental rotation behaviors in our physical model indicates the reliability and effectiveness of our proposed mechanisms. In addition to 80 nm AuNPs, we also demonstrated the orbital rotation of 80 nm silver nanoparticles (Figure S11 and Movie S5) and 200 nm AuNPs (Movie S6), showing the general applicability of OTNM. We further studied asymmetric nanoparticles with different geometries, such as gold nanocubes, gold nanorods, and Janus nanoparticles. However, light-driven rotation of these particles with a much higher asymmetry cannot be achieved because of the strong dependence of optical heating and the resultant forces on the particle orientation (Figure S12), which makes the restoration of particle orientation challenging.

Power Dependence of OTNM.

Last, we investigated the dependence of laser power on the rotation behaviors of OTNM (Figure 4). As discussed in Figure 2f, the rotation radius is the equilibrium position determined by the balance of optical force and thermocapillary force in the radial direction, which is independent of the laser power. Therefore, the experimental rotation radius of OTNM was in the range ~0.4–0.6 μm for a power range of ~1–10 mW (Figure 4a). The angular velocity of OTNM is dependent on the thermocapillary driving forces, which are related to the laser power, asymmetric geometry, and the equilibrium orientation of the AuNP. The experimental rotation rate was weakly correlated to the laser power with a slightly increasing trend (Figure 4b). This weak correlation arises from the different asymmetry of AuNPs, which causes a significant variation in the net thermocapillary driving force. To understand this correlation, we analyzed the theoretical rotation radius and angular velocity for different asymmetric AuNPs to account for the geometrical variations (Figure S5). The calculation results for all AuNPs are consistent with the experimental results, as indicated by the shaded areas in Figure 4. In addition, it should be noted that because of the random asymmetric geometries, there are large variations in the rotational behaviors

of AuNPs. For example, some AuNPs with certain geometries cannot stably rotate along the laser beam, which is also confirmed by numerical simulations. Meanwhile, the rotation of OTNM is randomly in the clockwise or counterclockwise direction (see Movie S7). Future studies on the statistics of the rotational behaviors of AuNPs are desired to further understand the underlying physics of OTNM.

CONCLUSIONS

In summary, we have developed opto-thermocapillary nanomotors that are operated on a solid substrate with suppressed Brownian motion. OTNM is driven by the synergy of optical forces and thermocapillary forces, in which the geometry of the nanoparticle plays an important role. We have further established a physical model to understand the origin of driving forces induced by the asymmetry of nanomotors, which sheds light on the rational design and optimization of optical nanomotors. In addition, the OTNM platform is promising for realization of light-driven rotation of more photothermal nanoparticles (e.g., silver and silicon) on other thermoresponsive substrates beyond CTAC films.

The OTNM provides many exciting possibilities in nanotechnological applications. It presents a design of nanoscale motors to fill the scale gap between molecular machines and microengines. OTNM can serve as fuel-free and gear-free rotary nanoengines for nanoelectro-mechanical systems to produce mechanical energy and perform work. The light-to-energy conversion efficiency of OTNM was estimated to be ~10^{-14} at a laser power of 5–10 mW (see Note S7), which is comparable with the state-of-the-art microscopic optical engines.[36] In comparison to other micro/nanomotors on solid substrates based on liquid-crystal films,[45–48] OTNM has no specific requirements for the solid substrate, making it compatible with current complementary metal-oxide-semiconductor technologies. Operating on solid substrates, OTNM can be integrated with solid-state nanoelectronics for the development of on-chip active nanodevices and applications in photonics, optoelectronics, and optomechanics.

METHODS

Materials Preparation.

CTAC (in powder form) was purchased from Chem-Impex. AuNPs (80 nm) and silver nanoparticles (AgNPs, 80 nm) were purchased from Sigma-Aldrich. To prepare the sample, 40 mL of CTAC solution (0.5 M) in isopropyl alcohol (IPA) was spin-coated onto a glass substrate. A thin layer of CTAC solid film with a thickness of ~200 nm was rapidly formed after IPA evaporation. Then, diluted AuNPs or AgNPs solution in ethanol was spin-coated on the as-prepared CTAC film for optical manipulation experiments.

Optical Setup.

The optical nanomotors experiments were conducted on an inverted microscope (Nikon TiE) with a ×100 oil objective (Nikon, numerical aperture: 0.5–1.3). A 660 nm laser (Laser Quantum) or a 532 nm laser (Coherent, Genesis MX STM-1 W) was expanded with a 5× beam expander (Thorlabs, GBE05-A) and directed to the microscope. An oil dark-field condenser (NA 1.20–1.43) and a color charge-coupled device (CCD, from Nikon) were used

for dark-field optical imaging. A fast monochromic CCD camera (Andor) was used to track the nanoparticles.

Characterizations.

All STEM images were taken with the Hitachi S5500 SEM/STEM system.

Measurement of Surface Tension.

The surface tension of quasi-liquid CTAC was measured using a high-sensitivity force-based tensiometer (Dataphysics DCAT 25). The measurement is based on a well-established Wilhelmy plate method.[49] An iridium–platinum plate (PT 11, length, 10 mm; width, 19.9 mm; thickness, 0.2 mm) was used as the Wilhelmy plate.

Supplementary Material

Refer to Web version on PubMed Central for supplementary material.

ACKNOWLEDGMENTS

Y.Z., J.L., P.S.K., K.Y., and Y.L. acknowledge financial support of the National Institute of General Medical Sciences of the National Institutes of Health (DP2GM128446) and the National Science Foundation (NSF-ECCS-2001650). J.L. also acknowledges the financial support of the University Graduate Continuing Fellowship from The University of Texas at Austin. We also thank the Texas Advanced Computing Center at The University of Texas at Austin (http://www.tacc.utexas.edu) for providing HPC resources that have contributed to the research results reported within this paper.

REFERENCES

(1). Hu C; Pané S; Nelson BJ Soft Micro- and Nanorobotics. Annu. Rev. Control Robot. Auton. Syst 2018, 1, 53–75.

(2). Novotný F; Wang H; Pumera M Nanorobots: Machines Squeezed between Molecular Motors and Micromotors. Chem 2020, 6, 867–884.

(3). Li J; Gao W; Dong R; Pei A; Sattayasamitsathit S; Wang J Nanomotor Lithography. Nat. Commun 2014, 5, 5026. [PubMed: 25248549]

(4). Manesh KM; Balasubramanian S; Wang J Nanomotor-Based 'Writing' of Surface Microstructures. Chem. Commun 2010, 46, 5704–5706.

(5). Wang J; Gao W Nano/Microscale Motors: Biomedical Opportunities and Challenges. ACS Nano 2012, 6, 5745–5751. [PubMed: 22770233]

(6). Li J; Esteban-Fernández de Ávila B; Gao W; Zhang L; Wang J Micro/Nanorobots for Biomedicine: Delivery, Surgery, Sensing, and Detoxification. Sci. Robot 2017, 2, No. eaam6431. [PubMed: 31552379]

(7). Wang J; Xiong Z; Zheng J; Zhan X; Tang J Light-Driven Micro/Nanomotor for Promising Biomedical Tools: Principle, Challenge, and Prospect. Acc. Chem. Res 2018, 51, 1957–1965. [PubMed: 30179455]

(8). Wu T; Nieminen TA; Mohanty S; Miotke J; Meyer RL; Rubinsztein-Dunlop H; Berns MW A Photon-Driven Micromotor Can Direct Nerve Fibre Growth. Nat. Photonics 2012, 6, 62–67.

(9). Ma X; Jannasch A; Albrecht U-R; Hahn K; Miguel-López A; Schäffer E; Sánchez S Enzyme-Powered Hollow Mesoporous Janus Nanomotors. Nano Lett 2015, 15, 7043–7050. [PubMed: 26437378]

(10). Uygun M; Singh VV; Kaufmann K; Uygun DA; de Oliveira SDS; Wang J Micromotor-Based Biomimetic Carbon Dioxide Sequestration: Towards Mobile Microscrubbers. Angew. Chem., Int. Ed 2015, 54, 12900–12904.

(11). Zhang L; Xiao Z; Chen X; Chen J; Wang W Confined 1D Propulsion of Metallodielectric Janus Micromotors on Microelectrodes under Alternating Current Electric Fields. ACS Nano 2019, 13, 8842–8853. [PubMed: 31265246]

(12). Jákli A; Senyuk B; Liao G; Lavrentovich OD Colloidal Micromotor in Smectic a Liquid Crystal Driven by DC Electric Field. Soft Matter 2008, 4, 2471–2474.

(13). Li J; Li T; Xu T; Kiristi M; Liu W; Wu Z; Wang J Magneto-Acoustic Hybrid Nanomotor. Nano Lett 2015, 15, 4814–4821. [PubMed: 26077325]

(14). Xu H; Medina-Sánchez M; Schmidt OG Magnetic Micromotors for Multiple Motile Sperm Cells Capture, Transport, and Enzymatic Release. Angew. Chem., Int. Ed 2020, 59, 15029–15037.

(15). Xu L; Mou F; Gong H; Luo M; Guan J Light-Driven Micro/Nanomotors: From Fundamentals to Applications. Chem. Soc. Rev 2017, 46, 6905–6926. [PubMed: 28949354]

(16). Sipova-Jungova H; Andren D; Jones S; Kall M Nanoscale Inorganic Motors Driven by Light: Principles, Realizations, and Opportunities. Chem. Rev 2020, 120, 269–287. [PubMed: 31869216]

(17). Dong R; Zhang Q; Gao W; Pei A; Ren B Highly Efficient Light-Driven TiO2-Au Janus Micromotors. ACS Nano 2016, 10, 839–844. [PubMed: 26592971]

(18). Qian B; Montiel D; Bregulla A; Cichos F; Yang H Harnessing Thermal Fluctuations for Purposeful Activities: The Manipulation of Single Micro-Swimmers by Adaptive Photon Nudging. Chem. Sci 2013, 4, 1420–1429.

(19). Zong Y; Liu J; Liu R; Guo H; Yang M; Li Z; Chen K An Optically Driven Bistable Janus Rotor with Patterned Metal Coatings. ACS Nano 2015, 9, 10844–10851. [PubMed: 26481901]

(20). Xu T; Soto F; Gao W; Garcia-Gradilla V; Li J; Zhang X; Wang J Ultrasound-Modulated Bubble Propulsion of Chemically Powered Microengines. J. Am. Chem. Soc 2014, 136, 8552–8555. [PubMed: 24898345]

(21). Wang W; Li S; Mair L; Ahmed S; Huang TJ; Mallouk TE Acoustic Propulsion of Nanorod Motors inside Living Cells. Angew. Chem., Int. Ed 2014, 53, 3201–3204.

(22). Chen C; Mou F; Xu L; Wang S; Guan J; Feng Z; Wang Q; Kong L; Li W; Wang J; Zhang Q Light-Steered Isotropic Semiconductor Micromotors. Adv. Mater 2017, 29, 1603374.

(23). Palacci J; Sacanna S; Vatchinsky A; Chaikin PM; Pine DJ Photoactivated Colloidal Dockers for Cargo Transportation. J. Am. Chem. Soc 2013, 135, 15978–15981. [PubMed: 24131488]

(24). Wang J; Xiong Z; Zhan X; Dai B; Zheng J; Liu J; Tang J A Silicon Nanowire as a Spectrally Tunable Light-Driven Nanomotor. Adv. Mater 2017, 29, 1701451.

(25). Wang H; Zhao G; Pumera M Beyond Platinum: Bubble-Propelled Micromotors Based on Ag and MnO_2 Catalysts. J. Am. Chem. Soc 2014, 136, 2719–2722. [PubMed: 24506544]

(26). Moo JGS; Presolski S; Pumera M Photochromic Spatiotemporal Control of Bubble-Propelled Micromotors by a Spiropyran Molecular Switch. ACS Nano 2016, 10, 3543–3552. [PubMed: 26919161]

(27). Lehmuskero A; Ogier R; Gschneidtner T; Johansson P; Käll M Ultrafast Spinning of Gold Nanoparticles in Water Using Circularly Polarized Light. Nano Lett 2013, 13, 3129–3134. [PubMed: 23777484]

(28). Shao L; Yang Z-J; Andrén D; Johansson P; Käll M Gold Nanorod Rotary Motors Driven by Resonant Light Scattering. ACS Nano 2015, 9, 12542–12551. [PubMed: 26564095]

(29). Yan Z; Scherer NF Optical Vortex Induced Rotation of Silver Nanowires. J. Phys. Chem. Lett 2013, 4, 2937–2942.

(30). Figliozzi P; Sule N; Yan Z; Bao Y; Burov S; Gray SK; Rice SA; Vaikuntanathan S; Scherer NF Driven Optical Matter: Dynamics of Electrodynamically Coupled Nanoparticles in an Optical Ring Vortex. Phys. Rev. E 2017, 95, 022604. [PubMed: 28298004]

(31). Liu M; Zentgraf T; Liu Y; Bartal G; Zhang X Light-Driven Nanoscale Plasmonic Motors. Nat. Nanotechnol 2010, 5, 570–573. [PubMed: 20601945]

(32). Bregulla AP; Yang H; Cichos F Stochastic Localization of Microswimmers by Photon Nudging. ACS Nano 2014, 8, 6542–6550. [PubMed: 24861455]

(33). Fränzl M; Muiños-Landin S; Holubec V; Cichos F Fully Steerable Symmetric Thermoplasmonic Microswimmers. ACS Nano 2021, 15, 3434–3440. [PubMed: 33556235]

(34). Peng X; Chen Z; Kollipara PS; Liu Y; Fang J; Lin L; Zheng Y Opto-Thermoelectric Microswimmers. Light: Sci. Appl 2020, 9, 141. [PubMed: 32864116]

(35). Chen Z; Li J; Zheng Y Heat-Mediated Optical Manipulation. Chem. Rev 2022, 122, 3122–3179. [PubMed: 34797041]

(36). Schmidt F; Magazzù A; Callegari A; Biancofiore L; Cichos F; Volpe G Microscopic Engine Powered by Critical Demixing. Phys. Rev. Lett 2018, 120, 068004. [PubMed: 29481280]

(37). Erbas-Cakmak S; Leigh DA; McTernan CT; Nussbaumer AL Artificial Molecular Machines. Chem. Rev 2015, 115, 10081–10206. [PubMed: 26346838]

(38). Lee T-C; Alarcón-Correa M; Miksch C; Hahn K; Gibbs JG; Fischer P Self-Propelling Nanomotors in the Presence of Strong Brownian Forces. Nano Lett 2014, 14, 2407–2412. [PubMed: 24707952]

(39). Li J; Liu Y; Lin L; Wang M; Jiang T; Guo J; Ding H; Kollipara PS; Inoue Y; Fan D; Korgel BA; Zheng Y Optical Nanomanipulation on Solid Substrates via Optothermally-Gated Photon Nudging. Nat. Commun 2019, 10, 5672. [PubMed: 31831746]

(40). Li J; Wang M; Wu Z; Li H; Hu G; Jiang T; Guo J; Liu Y; Yao K; Chen Z; Fang J; Fan D; Korgel BA; Alu A; Zheng Y Tunable Chiral Optics in All-Solid-Phase Reconfigurable Dielectric Nanostructures. Nano Lett 2021, 21, 973–979. [PubMed: 33372805]

(41). Fedoruk M; Lutich AA; Feldmann J Subdiffraction-Limited Milling by an Optically Driven Single Gold Nanoparticle. ACS Nano 2011, 5, 7377–7382. [PubMed: 21812459]

(42). Yang J; Zheng J; Ai R; Lai Y; Chow TH; Shao L; Wang J Plasmon-Enhanced, Self-Traced Nanomotors on the Surface of Silicon. Angew. Chem., Int. Ed 2021, 60, 24958–24967.

(43). Tian YC; Yu J; Gu M; Lian YD; Ai XQ; Tang TB Impedance Spectroscopic Study on Rotator and Disordered Phases in Trimethylammonium Chlorides. J. Phys. Chem. C 2016, 120, 23905–23909.

(44). Girot A; Danné N; Würger A; Bickel T; Ren F; Loudet JC; Pouligny B Motion of Optically Heated Spheres at the Water-Air Interface. Langmuir 2016, 32, 2687–2697. [PubMed: 26916053]

(45). Eelkema R; Pollard MM; Vicario J; Katsonis N; Ramon BS; Bastiaansen CWM; Broer DJ; Feringa BL Nanomotor Rotates Microscale Objects. Nature 2006, 440, 163–163. [PubMed: 16525460]

(46). Uchida E; Azumi R; Norikane Y Light-Induced Crawling of Crystals on a Glass Surface. Nat. Commun 2015, 6, 7310. [PubMed: 26084483]

(47). Kausar A; Nagano H; Ogata T; Nonaka T; Kurihara S Photocontrolled Translational Motion of a Microscale Solid Object on Azobenzene-Doped Liquid-Crystalline Films. Angew. Chem., Int. Ed 2009, 48, 2144–2147.

(48). Li J; Alfares A; Zheng Y Optical Manipulation and Assembly of Micro/Nanoscale Objects on Solid Substrates. iScience 2022, 25, 104035. [PubMed: 35313687]

(49). Wu N; Dai J; Micale FJ Dynamic Surface Tension Measurement with a Dynamic Wilhelmy Plate Technique. J. Colloid Interface Sci 1999, 215, 258–269. [PubMed: 10419660]

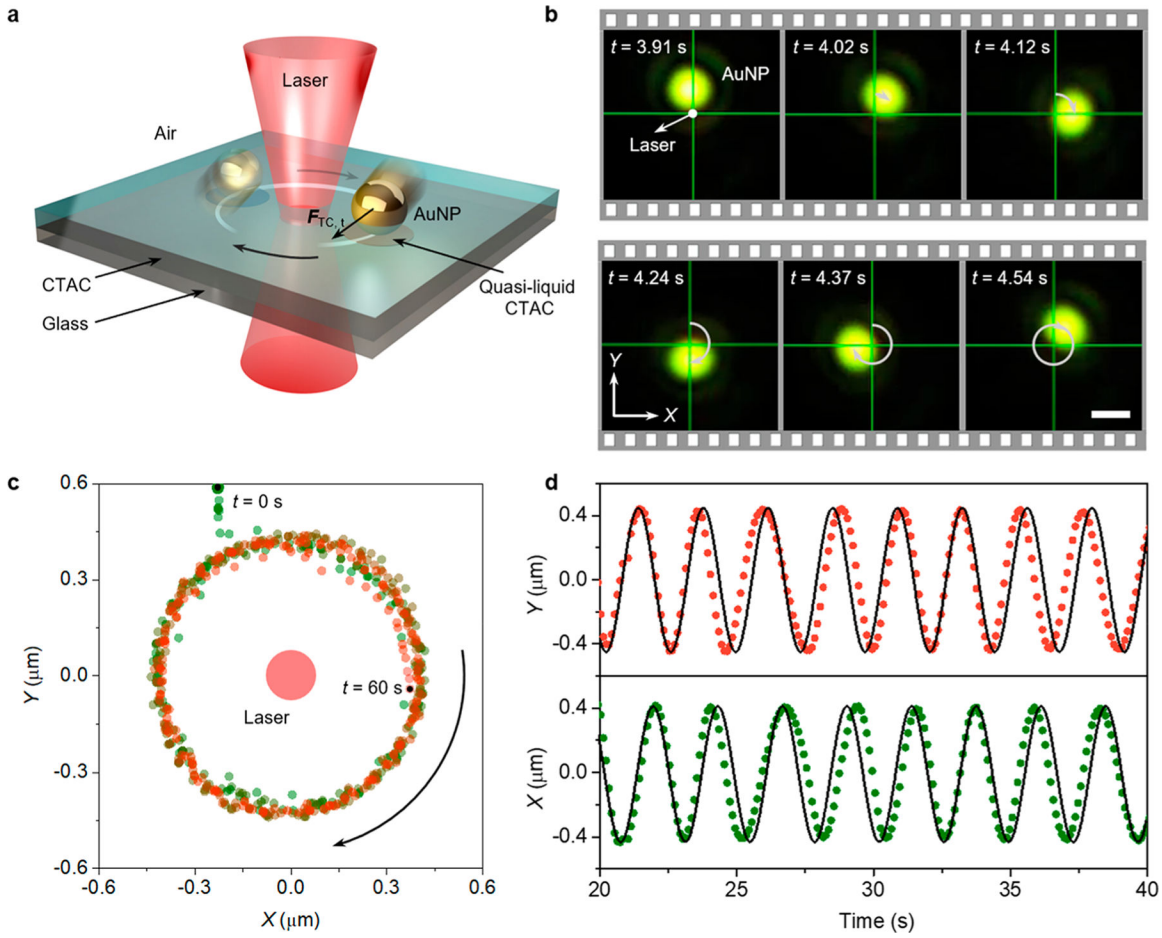

Figure 1.

General concept of OTNM. (a) Schematic of OTNM on a solid substrate. (b) Time-resolved dark-field optical images showing the orbital rotation of an 80 nm AuNP. Laser power: 6 mW. Scale bar: 1 μm. (c) Centroid tracking and (d) displacement of the rotating AuNP in (b). The origin of the coordinates is at the center of the laser beam. The curved arrows in (a)−(c) indicate the rotation direction of the nanomotor. The solid lines in (d) correspond to the sinusoidal fitting curves.

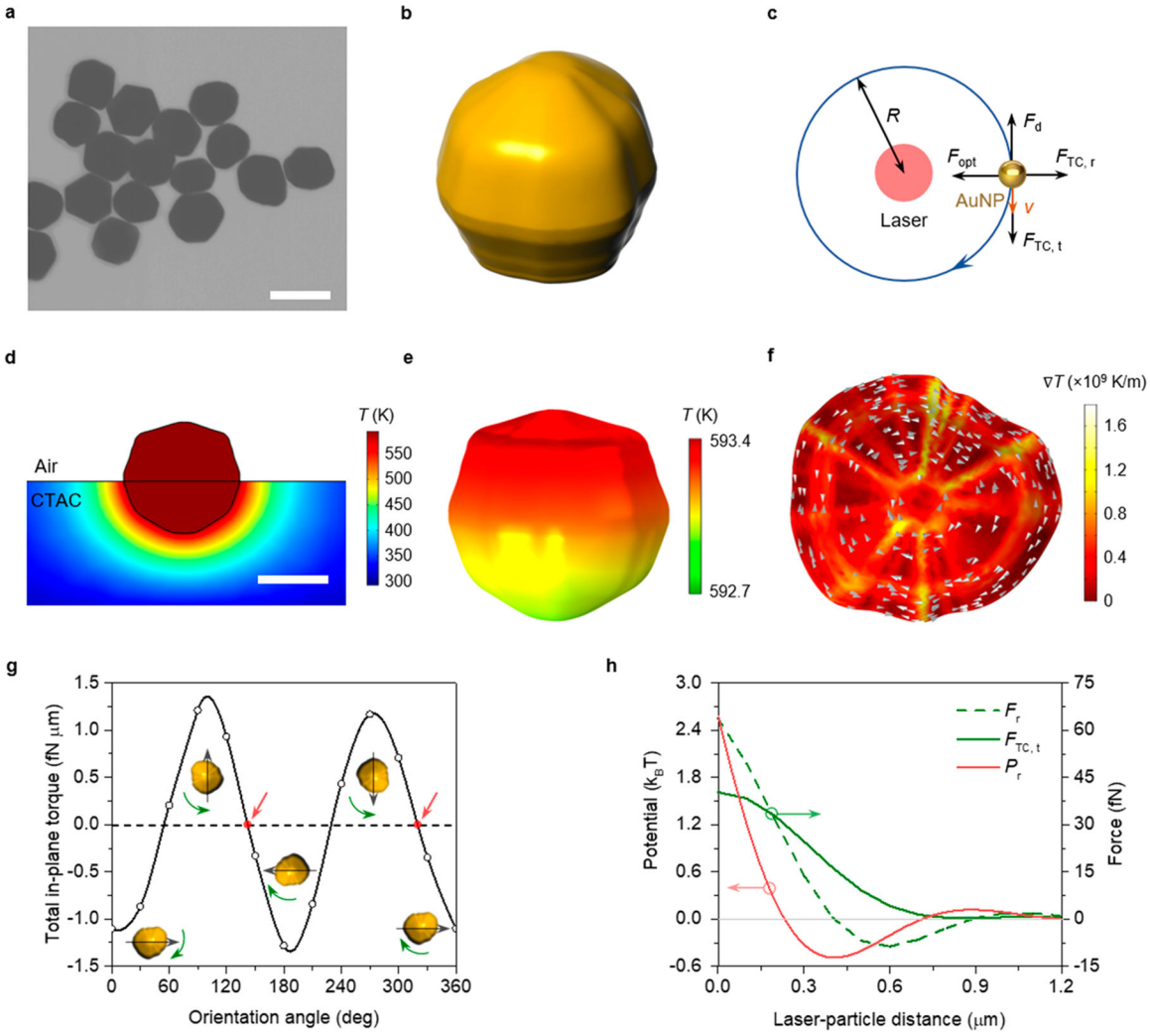

Figure 2.

Working principle of OTNM. (a) STEM image of 80 nm AuNPs used in experiments. Scale bar: 100 nm. (b) 3D reconstructed asymmetric AuNP based on STEM images, which is used for numerical simulations. (c) In-plane force analysis of OTNM. F_{opt} is optical force, F_d refers to resistant drag force, and $F_{TC,t}$ and $F_{TC,r}$ are the tangential and radial components of thermocapillary forces, respectively. (d) Simulated temperature distribution for an 80 nm AuNP under 660 nm laser illumination. Scale bar: 50 nm. (e) Close view of the temperature distribution at the AuNP surface. The laser power is 10 mW, and the laser–particle distance is 400 nm. (f) Simulated temperature gradient mapping (bottom view) on the surface of the AuNP under 660 nm laser irradiation (10 mW). The arrows indicate the in-plane temperature gradient parallel to the surface. (g) Calculated total in-plane torques as a function of the orientation angle of the AuNP. The red arrows show two equilibrium orientation angles where the torque equals zero. The black and green arrows indicate the orientation of the AuNP and the rotation direction at a certain orientation, respectively. (h) Calculated total forces in the radial direction (F_r), thermocapillary force in the tangential direction ($F_{TC,t}$) that is balanced by the resistant drag force, and the potential in the radial direction (P_r) as a function of laser–particle distance.

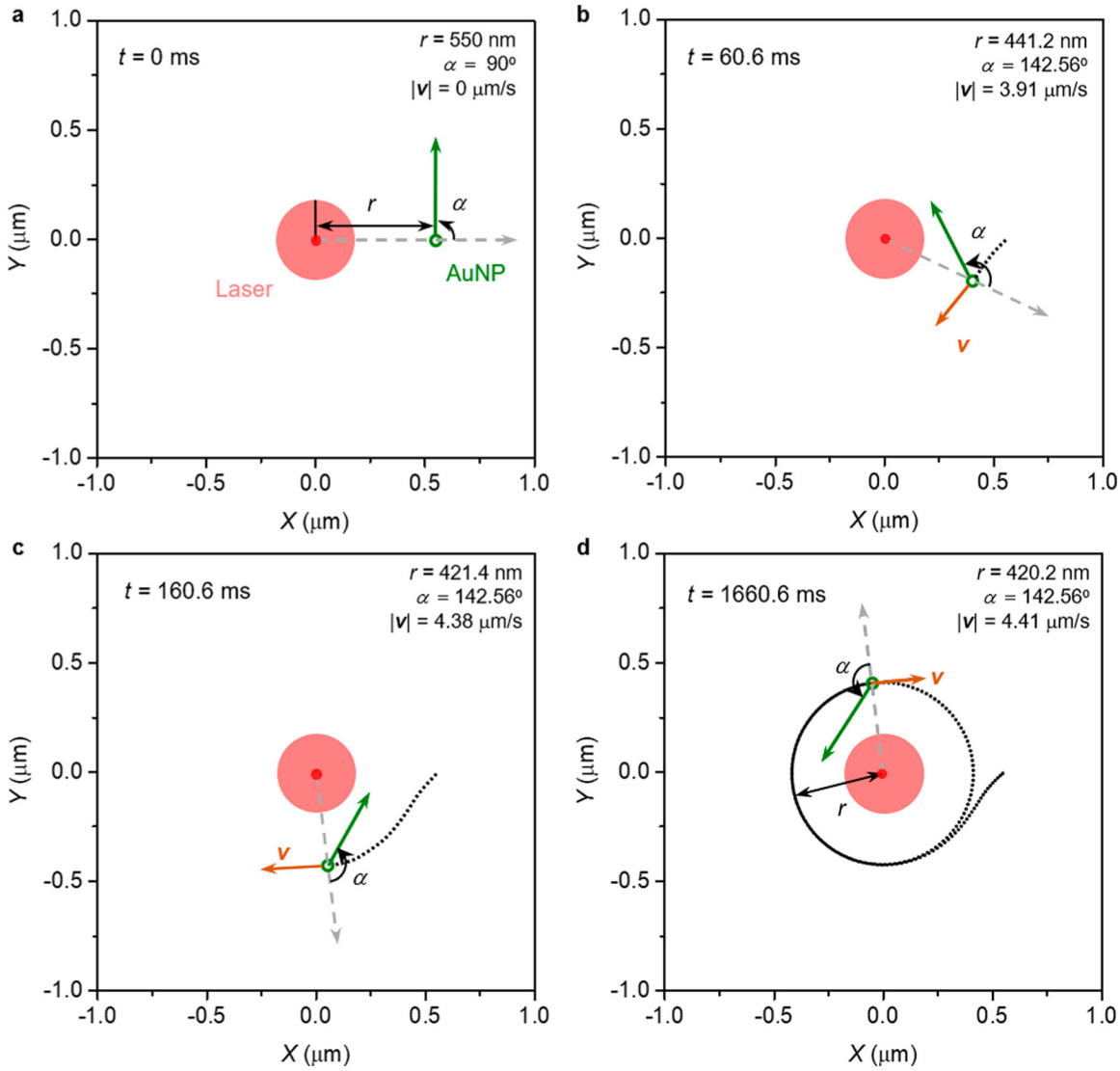

Figure 3.

Modeling of the motion of OTNM. (a) At the initial time, an asymmetric AuNP with a random orientation was placed at a laser−particle distance of 550 nm. All forces and torques based on numerical simulations were exerted on the AuNP. The green arrow indicates the orientation of the AuNP. r is the laser–particle distance, and α defines the orientation angle of the AuNP with respect to radial direction (gray dashed arrow). (b, c) The AuNP approached the circular orbit with reorientation at (b) t = 60.6 ms and (c) t = 160.6 ms. v is the instant velocity of the AuNP, and the black dot line shows the trajectory of the AuNP. (d) Steady rotation state of the AuNP.

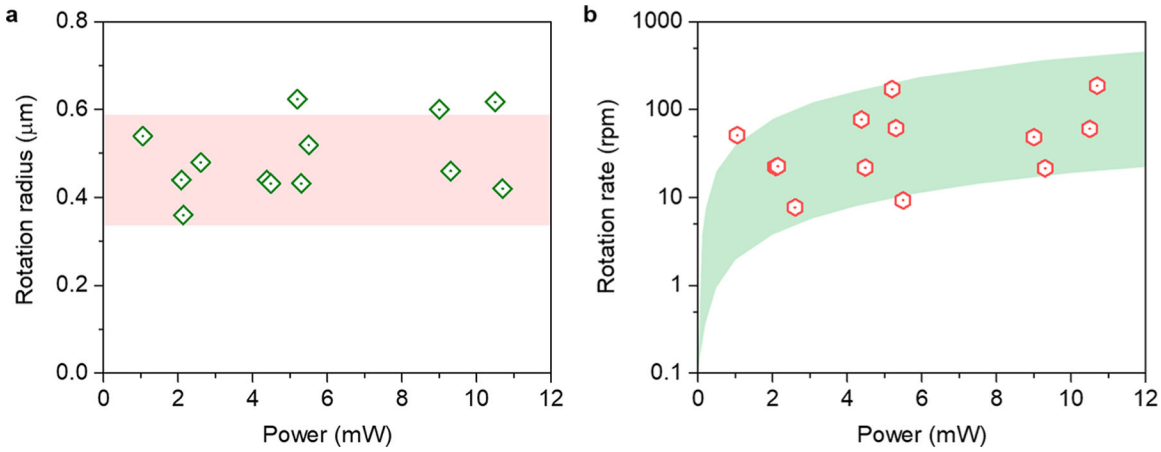

Figure 4.

Power-dependent rotation behaviors of OTNM. (a) Rotation radius and (b) rotation rate of OTNM as a function of laser power. The shaded areas correspond to the ranges obtained via the calculated theoretical values from different asymmetric AuNPs.